



# Flood Depth Estimation during Hurricane Harvey Using Sentinel-1 and UAVSAR Data

Sananda Kundu <sup>1,\*</sup>, Venkat Lakshmi <sup>2</sup> and Raymond Torres <sup>1,3</sup>

<sup>1</sup> Department of Geography, Manipur University, Imphal 795003, Manipur, India; torres@geol.sc.edu

<sup>2</sup> Department of Engineering Systems and Environment, University of Virginia, Charlottesville, VA 22904, USA; vlakshmi@virginia.edu

<sup>3</sup> Department of Earth and Ocean Science, University of South Carolina, Columbia, SC 29208, USA

\* Correspondence: skundu@geol.sc.edu or skundu@manipuruniv.ac.in

**Abstract:** In August 2017, Hurricane Harvey was one of the most destructive storms to make landfall in the Houston area, causing loss of life and property. Temporal and spatial changes in the depth of floodwater and the extent of inundation form an essential part of flood studies. This work estimates the flood extent and depth from LiDAR DEM (light detection and ranging digital elevation model) using data from the Synthetic Aperture Radar (SAR)–Unmanned Aerial Vehicle Synthetic Aperture Radar (UAVSAR) and satellite sensor—Sentinel-1. The flood extent showed a decrease between 29–30 August and 5 September 2017. The flood depths estimated using the DEM were compared with the USGS gauge data and showed a correlation ( $R^2$ ) greater than 0.88. The use of Sentinel-1 and UAVSAR resulted in a daily temporal repeat, which helped to document the changes in the flood area and the water depth. These observations are significant for efficient disaster management and to assist relief organizations by providing spatially precise information for the affected areas.

**Keywords:** Harvey; UAVSAR; Sentinel-1; flood extent; depth; LiDAR DEM



**Citation:** Kundu, S.; Lakshmi, V.; Torres, R. Flood Depth Estimation during Hurricane Harvey Using Sentinel-1 and UAVSAR Data. *Remote Sens.* **2022**, *14*, 1450. <https://doi.org/10.3390/rs14061450>

Academic Editors: Teodosio Lacava and Seon Ki Park

Received: 30 December 2021

Accepted: 15 March 2022

Published: 17 March 2022

**Publisher's Note:** MDPI stays neutral with regard to jurisdictional claims in published maps and institutional affiliations.



**Copyright:** © 2022 by the authors. Licensee MDPI, Basel, Switzerland. This article is an open access article distributed under the terms and conditions of the Creative Commons Attribution (CC BY) license (<https://creativecommons.org/licenses/by/4.0/>).

## 1. Introduction

Floods are natural hazards that cause significant damage to property and infrastructure. Flood events are considered one of the most fatal and costliest natural disasters, and a total damage of over \$1 trillion and deaths of 220,000 have been recorded since 1980 throughout the globe [1]. In 2020, about 22 weather–water–climate disaster events struck the United States, and each of them resulted in losses of more than \$1 billion [2]. Modern remote sensing analyses of recent flooding can provide substantial benefits to society, such as predicting locations of infrastructure disruption or loss and aid in the adoption of evacuation routes for a range of flood-prone landscapes [3]. Moreover, a real-time assessment of flood extent and depth is essential for the optimal use of rescue resources, the delivery of emergency supplies, and immediate recovery measures. The airborne Synthetic Aperture Radar (SAR) from the Jet Propulsion Laboratory (JPL) provides near-real-time flood mapping as the data are unaffected by weather conditions [4].

The majority of the literature reporting SAR-based hydrologic analyses has focused on flood inundation in forested wetlands [4,5]. Most of these studies focus on the areal extent of inundation, and only a handful address water level and spatial changes. In particular, Alsdorf et al. [6] examined the water level dynamics along parts of the Amazon floodplain and found that SAR could be used to reliably measure changes in the water level in vegetation inundated areas. Brown et al. [7] estimated the flood boundary from SAR observations and flood surface elevation using a digital terrain model derived from LiDAR observations to obtain flood depths. Many previous works emphasized the change and impact of extreme precipitation during Harvey with respect to modeled and ground data [8–11]. The impact of urbanization on rainfall and increased flooding has also been assessed during Harvey [12].

Most studies of flood depth, extent, and water level dynamics rely on either L (1.5 GHz)- or C (6.6 GHz)-band. L-band is better suited to identifying water in forested areas as compared with C-band; however, for sparsely vegetated areas and in leaf-off conditions, C- or X-band (10 GHz) data are also suitable for mapping [13]. Hurricane Harvey was a category 4 storm that caused extensive flooding in the highly urbanized and low-lying areas of Houston, Texas, on 29–30 August 2017 of up to 1.5 m [14], resulting in one of the most disastrous occurrences of urban flooding in United States [9,15,16]. Here we estimate the extent and depth of flooding caused by Hurricane Harvey using real-time SAR data. The main objectives of this work are to (i) estimate the flood extent during Hurricane Harvey and (ii) estimate flood depth. We hypothesize that radar signals provide insight into flood extent and depth in an urban setting. This is significant as during floods insitu sensors may become nonoperational due to submergence. Hence, radar remote sensing is a viable approach to study both urban and nonurban flooding.

## 2. Materials and Methods

### 2.1. Site Properties and Conditions

The study site is the greater Houston area, a densely populated urban–rural region with an area of about 4692 km<sup>2</sup> (Figure 1). The study time period is focused on flooding during and after the passing of Hurricane Harvey from 29 August to 5 September 2017. The spatial and temporal variability of daily precipitation from Global Precipitation Measurements (GPM) from August 24 to 31 is illustrated in Figure 2 (<https://pmm.nasa.gov/data-access/downloads/gpm> accessed on 1 October 2017).

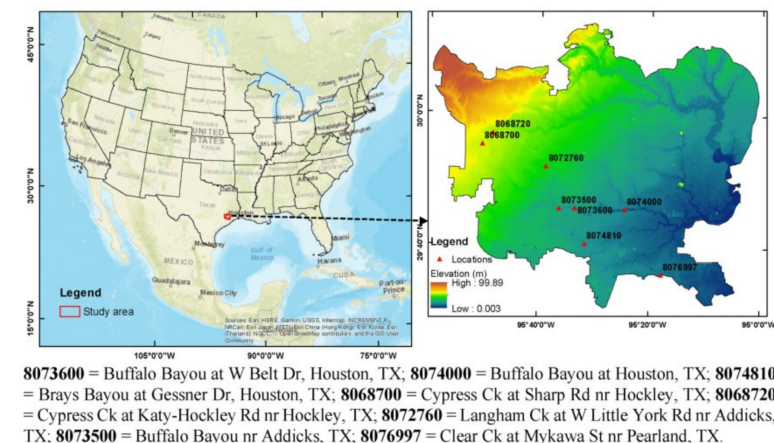


**Figure 1.** Study area with elevation and gauge locations.

Throughout the greater Houston area, the daily precipitation intensity varied from 10 mm/day to greater than 100 mm/day from 25–29 August 2017. Hurricane Harvey precipitation led to maximum flooding on 27 August [17]. The precipitation associated with Hurricane Harvey started on 25 August, peaked on 28 August, and persisted until 30 August 2017, causing extensive flooding [8]. This study is focused on the period from 29 August through 2 September and 5 September 2017. The LiDAR DEM data were obtained from the Texas Natural Resources Information System (TNRIS, <https://tnris.org/data-download/#!/statewide> accessed on 1 November 2017) at a spatial resolution of 1 m.

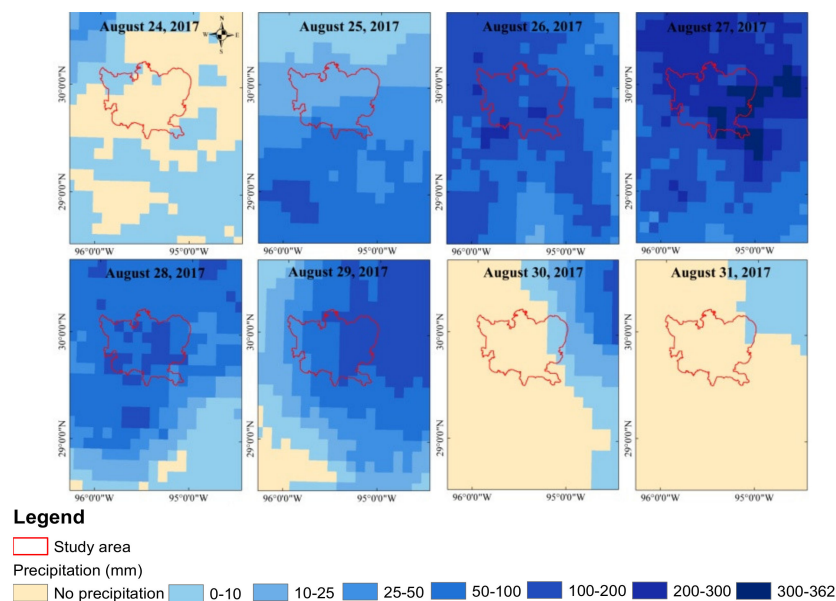


**Figure 2.** Spatial distribution of daily precipitation over Houston and surrounding areas from GPM observations (24–31 August 2017).

## 2.2. Data and Processing

Our analyses make use of the LiDAR DEM and SAR data to estimate inundation depth and extent. The Sentinel-1 data were obtained from the ASF Earthdata site (<https://vertex.daac.asf.alaska.edu/#> accessed on 1 September 2017). The Sentinel-1 data are obtained from two satellites in the same orbital plane, Sentinel-1A and Sentinel-1B (<https://Sentinel.esa.int/web/Sentinel/missions/Sentinel-1/overview> accessed on 1 October 2017). Sentinel-1 is an airborne repeat-pass interferometric observation system with a 16 km swath. It is a C-band system developed by the European Space Agency. The Sentinel-1 products are useful for flood monitoring due to their frequent revisit time (6 days). Three Sentinel-1A and 1B level-1 observations of the Ground Range Detected (GRD) were used as follows: 29 August (ascending orbit), 30 August and 5 September (descending orbit). The observations with the peak flood levels helped in the estimation of flood extent and depth. VV polarized backscatter data show higher variability over land and lower variability over vegetated areas that could be considered water [5] and, therefore, were used in this study. VV is like-polarized, where transmit and receive polarizations are the same, and VH is cross-polarized where transmit and receive polarizations are orthogonal to each other (<https://www.nrcan.gc.ca/node/9567> accessed on 1 October 2017). The level1 data of Sentinel-1 were used in this study, and speckle correction was performed to remove the noise [18].

The JPL UAVSAR observations covered the entire city and surrounding areas operating at a 1.26 GHz frequency (<https://uavsar.jpl.nasa.gov/cgi-bin/data.pl> accessed on 1 October 2017). UAVSAR is used in this study as it has a high spatial resolution ( $1.8 \text{ m} \times 0.8 \text{ m}$ ) and long wavelength (23.8 cm) [19]. The UAVSAR data from the NASA L-band airborne SAR provide repeat-track interferometric observations from a pod-mounted polarimetric instrument originally designed to operate on an unmanned aerial vehicle (UAV) at an altitude of 13,800 m with a bandwidth of 80 MHz (<https://directory.eoportal.org/web/eoportal/airborne-sensors/uavsar> accessed on 1 October 2017). An InSAR pair of GRD data with HH polarization was used. The HH polarization of UAVSAR was used to identify the flooded area as it can penetrate the canopy, and it has a good contrast between land and water [20]. Additionally, in windy conditions, the backscatter of HH is lower on rough surfaces than the VV polarization [21]. Preprocessing of the Sentinel-1 data was carried out with VV polarization with GRD mode and for UAVSAR with HH polarization. Amplitude images of UAVSAR and Sentinel-1 were georeferenced and are transformed to backscatter

values for the identification of the flooded and nonflooded areas [22]. These processed images were used to estimate the extent of floodwater using the threshold method [12]. Details of the data are provided in Table 1.

**Table 1.** Data properties.

Properties	Sentinel-1 (29–30 August and 5 September)	UAVSAR (31 August and 1–2 September)	LiDAR DEM
Resolution	5 × 20 m (range × azimuth)	1.8 m × 0.8 m (range × azimuth)	
Swath width	250 (IWS) km	16 km	1 m (spatial resolution)
Polarization	VV and VH	Full quad-polarization	
Organization	ESA	NASA	
Band	C	L	

Source of UAVSAR: <https://directory.eoportal.org/web/eoportal/airborne-sensors/uavsar> accessed on 1 October 2017.

The backscatter coefficient ( $\sigma_0$ ), expressed in decibels (dB), provides information for the identification of surface water. With C-band VV polarization, the backscatter coefficient varies between  $-6$  and  $-15$  dB for water, while in VH polarization varies between  $-15$  and  $-24$  dB [22]. Flooded area extraction using backscatter observations relies on a threshold-based methodology, which requires careful identification of the threshold backscatter values. Water surface identification from Sentinel-1 data was carried out using the method of [23].

Global precipitation measurement (GPM) data are used in the study, which is an international satellite mission and launched by National Aeronautics and Space Administration (NASA) and the Japan Aerospace Exploration Agency (JAXA) [24]. The GPM products provide precipitation for every 30 min, and the spatial resolution is  $0.1^\circ \times 0.1^\circ$ , covering the globe's  $60^\circ\text{N}$ – $60^\circ\text{S}$  region. To evaluate the total precipitation that occurred during Harvey, GPM rainfall distribution from 24 to 31 August was presented.

### 2.3. Estimation of Flood Depth Using Flood Extent and DEM

LiDAR DEM observations were used to determine the flood depth using the extent of the flooded area [25]. High-resolution DEMs were used in many studies using different elevation, slope, and aspect studies [26], especially LiDAR [27,28]. The LiDAR DEM-based depths were compared with the corresponding U.S. Geological Survey's (USGS) gauge observations with the North American Vertical Datum of 1988 (NAVD 88) as the vertical reference. Flood depth estimations were carried out using elevation from the LiDAR DEM and flood extent. We estimated the flood depth by calculating the difference in the elevation obtained from flood extent boundaries and their corresponding elevation values from LiDAR DEM. To further elaborate, this was performed by extracting the boundary cells of the flooded area and assigning their DEM elevations to the surrounding area by iteration [25]. The permanent water bodies were identified from a Landsat image during a nonflooded time period (April) using the normalized difference water index (NDWI) method. The threshold method was used to differentiate between flooded and nonflooded areas [12] of Sentinel-1 and UAVSAR observations.

## 3. Results

The distribution of precipitation over the study area obtained from the Global Precipitation Measurement (GPM) data from August 24 to 30 is displayed in Figure 2. The precipitation over Houston started on 24 August and increased from 10 mm/day to more than 100 mm/day on 27 August, and heavy rainfall continued till 29 August. The precipitation decreased and ceased after 29 August in most of the area.

The precipitation distribution is reflected in the observed gauge heights in the area. Variations in gauge heights, rainfall, and discharge were observed in the different USGS gauges that are distributed throughout the Houston area, which are shown in Figure 3, during the passage of Hurricane Harvey. The horizontal axis indicates dates from 23 August to 10 September 2017. The gauge heights and discharge reach the highest level on 27–28 August. In all the gauges, there is a short lag-time, and the peak discharge and gauge height are reached after the rainfall begins and reaches its maximum on 27 August. There are missing data for one gauge (Gauge ID: 8074810), but all the gauges are showing similar timing of floodwater peak or discharge. The gauge height drops immediately after the cessation of rainfall on 29 September 2017. The maximum height is reached suddenly on August 27 or 28 due to highest rainfall on 27 September, and again it drops almost immediately after the cessation of rainfall.

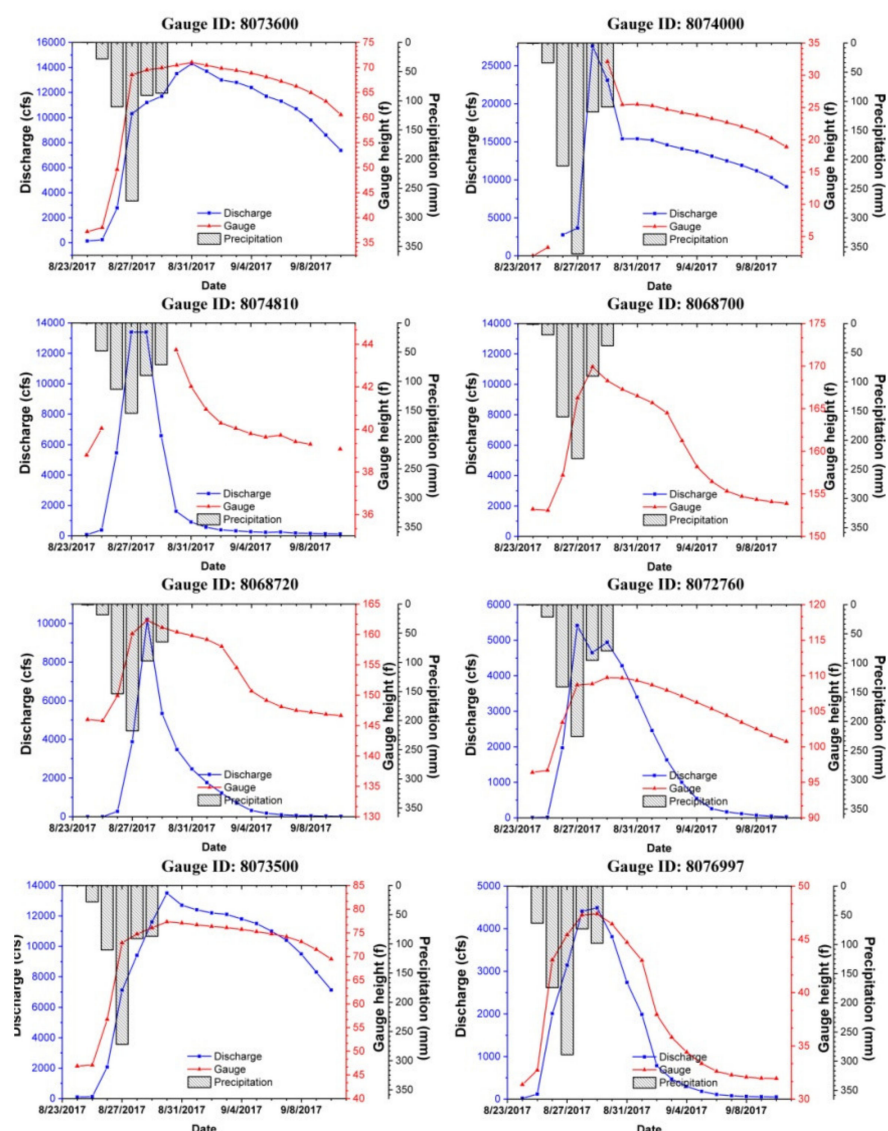


**Figure 3.** Precipitation, gauge heights, and discharge during the passage of Hurricane Harvey.

### 3.1. Flood Extent

The flood extent due to Hurricane Harvey is from 29 August to 5 September 2017 is illustrated in Figure 4. As observed from the August 29 and 30 images, these were peak flood days, while 5 September showed the least amount of flooding. The extent of the flooded area for 29 August was patchy, but the most continuous flooding occurred

over western Houston, which includes urban and rural areas. The 30 August 2017 map shows a 1.22% increase in flood extent, indicating the maximum area affected by flood. However, a decrease in precipitation after 29 August 2017 resulted in a gradual decrease in the water levels. The precipitation stopped after 29 August 2017. Therefore, recession of water was observed on 31 August as a decline in water extent and retreat from the city center, although water was retained in the outskirts of Houston in the rural areas. The floodwaters receded after 24–48 h in most of the areas, but a few areas showed elevated water levels for several days after the hurricane (Figure 4). The decrease in the flood extent on 1 September was greater than that of the extent from 31 August 2017 and continued to decline through September 2 and 5. The total flooded area with a peak flooded area of 12.92% on 30 August 2017 gradually reduced to 11.09% on 31 August 2017, 10% on 1 September 2017, and 3.82% and 1.30% on 2 and 5 September 2017, respectively, in both Sentinel-1 and UAVSAR images (Table 2).

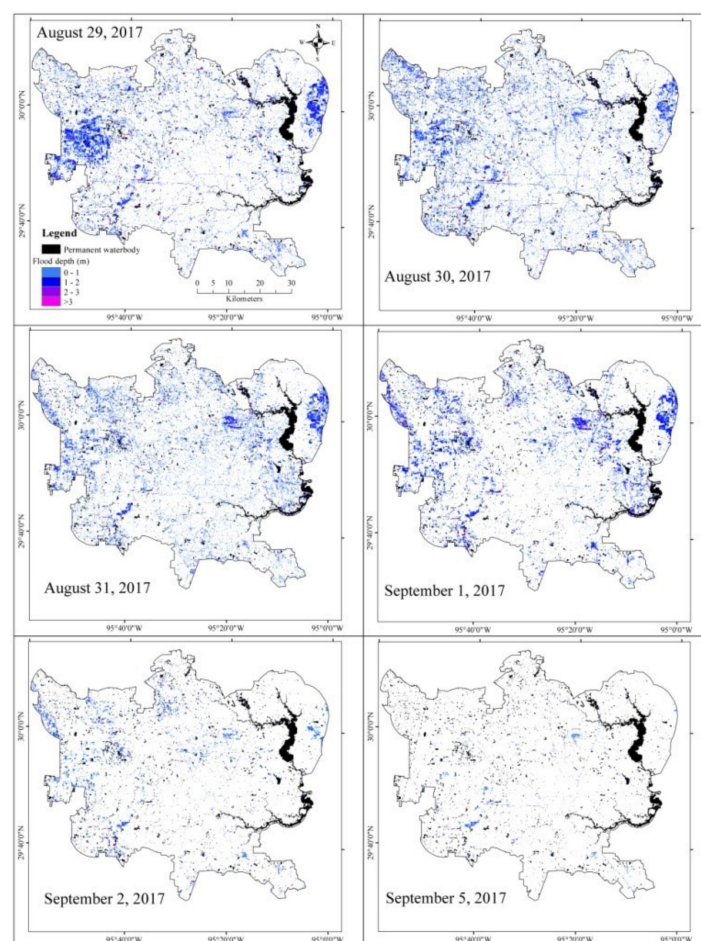


**Figure 4.** Flood extent and depth derived using Sentinel-1 and UAVSAR using LiDAR DEM and extent.

**Table 2.** Area of varying floodwater depths using calculated depth from DEM.

Depth of Floodwater	29 August	30 August	31 August	1 September	2 September	5 September
Depth below 1 m in respect to total area (%)	8.19	10.13	9.12	6.75	3.23	1.14
Depth below 2 m in respect to total area (%)	10.90	12.21	10.70	9.28	3.60	1.21
Total flooded area	11.70	12.92	11.09	10.00	3.82	1.30

### 3.2. Flood Depth Estimation Using DEM

The spatial distribution of flood depths was estimated using the flood extent and the LiDAR DEM (Figure 4). Depth estimation by this method indicated a 0 to 2 m level of variability (more than 22% of the total study area on 30 August) over most of the inundated area of Houston for all days. However, errors in the estimation process were observed as negative values of depth, which indicated no flood inundation or depth in the area. This posed as a limitation of this method. SAR data from August 25 to 28 were not available during the maximum rainfall, hindering the inundation estimation during the peak flood day. We estimated areas with a depth below 2 and 1 m for the total study area (Table 2). On 29 and 30 August 2017, the depth was highest, with many areas experiencing 1–2 m depths, and a few areas along the perimeter of the main flooded areas had 0–1 m depths. The flood map on 29 August 2017 indicated 8.19% areas of <1 m depth and 10.90% areas of <2 m depth and, for August 30, showed an increase in the <1 m depth area of 10.13% and 12.21% of areas of <2 m depth. The city center experienced <1 m depth, while the western and northeast borders showed major flooding. Examination of the flooding for 31 August 2017 showed a decrease in flood extent and depth (total flooded area was 11.09%, which was about 1.83% less than August 30), 1 and 2 September 2017 indicated flood recession and lower depths in the center of the city (3.6% area of <2 m depth on September 2 compared to 10.7% on August 31), and scattered areas of floodwater were noticed on 5 September 2017 (1.30% of total area) (Table 2). The extent and depth of floodwater with respect to the original images of 30 August 2017 are illustrated in Figure 5, depicting different areas of flooding. The SAR amplitude images are shown in Figure 5A, and the areas of inundation and depth variation are shown in Figure 5B,C, respectively. The intersection of roads on top of the figure varied from <1 to 2 m along the roads, and the bottom figure is indicated by the Barker Reservoir and George Bush Park, which showed inundation of <1 to more than 3 m of depth. The area indicated in Figure 5A2 and Addicks (neighborhood area) were reported under inundation for weeks [17]. Gebremichael et al. [29] assessed the flood distribution using Sentinel-1 data and showed more flooding in the outskirt area of the city.

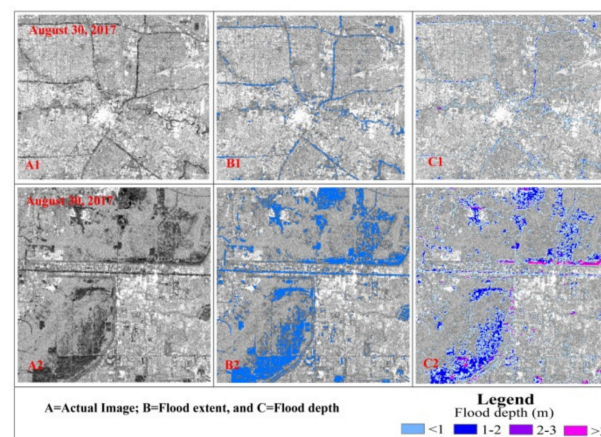


**Figure 5.** Flooded areas' extent and depth for 30 August 2017 (original SAR image and estimated extent and depth). Figures (A1–C1) indicate the Sentinel-1 image and corresponding extent and depth in (A2–C2), respectively, for two different locations.

The depths obtained from LiDAR DEM by the process of differencing water surface elevation and land surface elevation (i.e., DEM) were compared with the observed depth from USGS gauges (Figure 6), and kappa statistics and the overall accuracy of this method were estimated for flooded points between USGS data and the flood extent (Table 3). The Pearson correlation ( $R^2$ ) for all dates for gauges with positive values or floodwater was greater than 0.88. The kappa statistic ranged from 0.90 to 1, and the overall accuracy was 96% to 100% for these gauge stations. This method of flood depth estimation was essential (especially during flooding when gauges may be under water or in areas with little or no

insitu observations) since it involved the use of the extent and the DEM [25], hence, the depth estimation at all available dates during the passage of the hurricane.

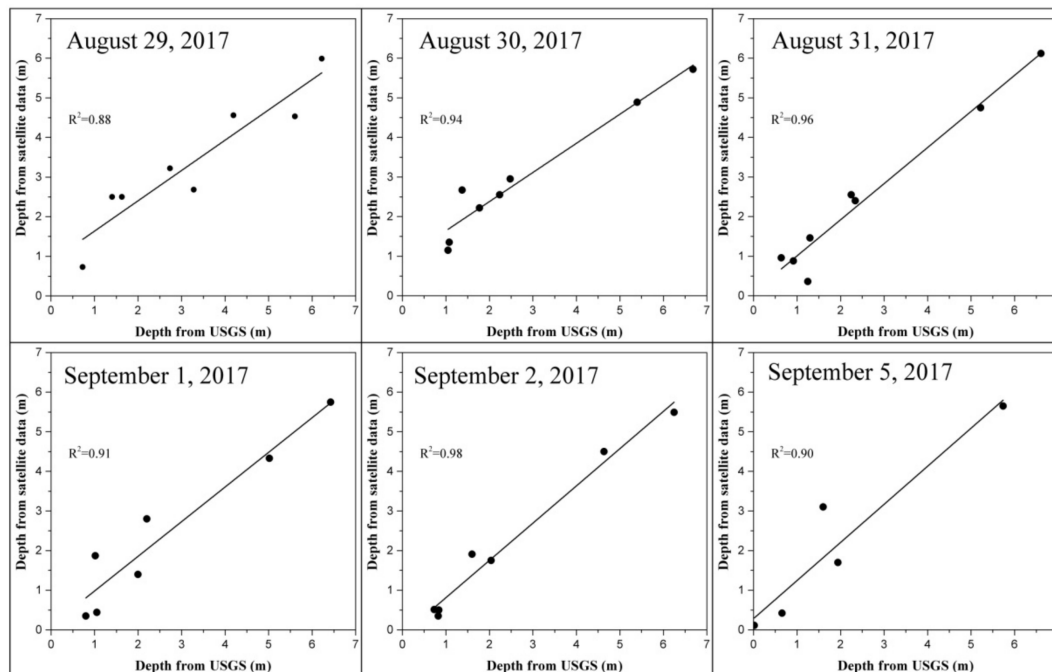


Figure 6. Comparison of depth of flood derived from DEM with USGS gauge observations.

Table 3. Kappa and overall accuracy between USGS data and estimated flood from SAR data.

Type	29 August	30 August	31 August	1 September	2 September	5 September
Overall accuracy	0.96	0.96	1	1	0.96	1
Kappa	0.91	0.91	1	1	0.90	1

#### 4. Conclusions

The present work provided an estimate of the extent and depth of flooding during the passage of Hurricane Harvey over Houston and the surrounding areas. The spatial and temporal variations of the depth of the floodwater during the storm were mapped using this event. The flood extent for the 6 days during Hurricane Harvey was estimated using Sentinel-1 and UAVSAR data, which showed a gradual decrease from 29–30 August 2017 to 5 September 2017. A lesser flood extent in the main part of Houston was observed, while the fringe areas showed a greater extent of flooding. The flood depth was estimated using a LiDAR DEM and flood extent, which indicated a depth of <1 to 3 m. The depth of the water decreased with time, and floodwater started receding when the precipitation stopped after 29 August 2017. A total area of less than 1 m in depth covered the maximum areal extent on 30 August 2017, followed by 31 and 29 August 2017, and September 1, 2, and 5, 2017. An area of flood depth of less than 2 m in depth was greatest on 30 August 2017, followed by 29 and 31 August 2017. The area of greater flood depth decreased gradually on September 1, 2, and 5, 2017. The total flooded area, as observed from Sentinel-1 and UAVSAR data, was highest on 30 August 2017 (12.92%), followed by 29 and 31 August 2017 and September 1, 2, and 5, 2017. The flood depth observations of the 6 days were compared with the USGS gauge data, which showed a correlation ( $R^2$ ) of greater than 0.88 in various gauge locations, and the overall accuracy in identifying the flooded and nonflooded areas performed well for the locations of gauges in the region. Smaller areas of the flooding were noticed in the west and northeast of the city. This method was particularly important for the mapping of the flood extent and depth in areas with little or no insitu observations.

Identifying the floodwater extent and depth within the city area with real-time SAR images can help in the adoption of an effective land use management strategy to limit the damage during heavy precipitation associated with hurricane activity in the future.

Future studies can use precipitation from satellite sensors that have been extensively validated using insitu observations in Vietnam (Sutton et al.), the United States [30], and India [31] or using rainfall as inputs to hydrological models [32] and an integrated assessment of the hydrological extremes [33,34]. Perhaps the best advances will arise when the state of the land surface wetness can be mapped in high spatial resolution [35] using the theory of thermal inertia [36–40]. With the initial state of the soil wellcharacterized, the flooding can be better predicted by observations and models.

**Author Contributions:** Conceptualization, V.L., R.T. and S.K.; methodology, S.K.; software, S.K.; formal analysis, V.L., R.T. and S.K.; writing—original draft preparation, S.K.; writing—review and editing, V.L. and R.T.; supervision, V.L.; funding acquisition, R.T. and V.L. All authors have read and agreed to the published version of the manuscript.

**Funding:** Financial support for this work was received from NASA (grant no. NASA SC EPSCoR award NNX16AR02A).

**Institutional Review Board Statement:** Not applicable.

**Informed Consent Statement:** Not applicable.

**Data Availability Statement:** Not applicable.

**Acknowledgments:** The authors are thankful to JPL, NASA, for the UAVSAR data and the European Space Agency (ESA) for the Sentinel-1 data. The Texas Natural Resources Information System (TNRIS) provided the LiDAR DEM, and the United States Geological Survey (USGS) provided gauge data.

**Conflicts of Interest:** The authors declare no conflict of interest.

## References

1. Munich Re. NatCatSERVICE. 2018. Available online: <https://natcatservice.munichre.com/> (accessed on 1 December 2020).
2. NOAA National Centers for Environmental Information. U.S. 2020 Billion-Dollar Weather and Climate Disasters. 2020. Available online: <https://www.ncdc.noaa.gov/billions/> (accessed on 1 December 2021).
3. Smith, D.I. Flood damage estimation—a review of urban stage-damage curves and loss functions. *Water SA* **1994**, *20*, 231–238.
4. Amitrano, D.; Di Martino, G.; Iodice, A.; Riccio, D.; Ruello, G. Unsupervised rapid flood mapping using sentinel-1 GRD SAR images. *IEEE Trans. Geosci. Remote Sens.* **2018**, *56*, 3290–3299. [[CrossRef](#)]
5. Twele, A.; Cao, W.; Plank, S.; Martinis, S. Sentinel-1-based flood mapping: A fully automated processing chain. *Int. J. Remote Sens.* **2016**, *37*, 2990–3004. [[CrossRef](#)]
6. Alsdorf, D.E.; Smith, L.C.; Melack, J.M. Amazon floodplain water level changes measured with interferometric sir-c radar. *IEEE Trans. Geosci. Remote Sens.* **2001**, *39*, 423–431. [[CrossRef](#)]
7. Brown, K.M.; Hambidge, C.H.; Brownett, J.M. Progress in operational flood mapping using satellite synthetic aperture radar (sar) and airborne light detection and ranging (LiDAR) data. *Prog. Phys. Geogr.* **2016**, *40*, 196–214. [[CrossRef](#)]
8. Van Oldenborgh, G.J.; van der Wiel, K.; Sebastian, A.; Singh, R.; Arrighi, J.; Otto, F.; Hausteijn, K.; Li, S.; Vecchi, G.; Cullen, H. Corrigendum: Attribution of extreme rainfall from hurricane Harvey, august 2017 (2017 *Environ. Res. Lett.* 12 124009). *Environ. Res. Lett.* **2018**, *13*, 019501. [[CrossRef](#)]
9. Risser, M.D.; Wehner, M.F. Attributable human-induced changes in the likelihood and magnitude of the observed extreme precipitation during hurricane Harvey. *Geophys. Res. Lett.* **2017**, *44*, 12–457. [[CrossRef](#)]
10. Emanuel, K. Assessing the present and future probability of Hurricane Harvey’s rainfall. *Proc. Natl. Acad. Sci. USA* **2017**, *114*, 12681–12684. [[CrossRef](#)]
11. Sarkar, S.; Singh, R.P.; Chauhan, A. Anomalous changes in meteorological parameters along the track of 2017 Hurricane Harvey. *Remote Sens. Lett.* **2018**, *9*, 487–496. [[CrossRef](#)]
12. Zhang, B.; Wdowinski, S.; Oliver-Cabrera, T.; Koirala, R.; Jo, M.; Osmanoglu, B. Mapping the extent and magnitude of severe flooding induced by Hurricane IRMA with multi-temporal SENTINEL-1 SAR and InSAR observations. *Int. Arch. Photogramm. Remote Sens. Spatial Inf. Sci.* **2018**, *42*, 2237–2244. [[CrossRef](#)]
13. Plank, S.; Jüssi, M.; Martinis, S.; Twele, A. Mapping of flooded vegetation by means of polarimetric sentinel-1 and alos-2/palsar-2 imagery. *Int. J. Remote Sens.* **2017**, *38*, 3831–3850. [[CrossRef](#)]
14. Lin, L.; Weng, F. Estimation of hurricane maximum wind speed using temperature anomaly derived from advanced technology microwave sounder. *IEEE Geosci. Remote Sens. Lett.* **2018**, *15*, 639–643. [[CrossRef](#)]
15. NOAA. 2017. Available online: [https://www.weather.gov/crp/hurricane\\_harvey](https://www.weather.gov/crp/hurricane_harvey) (accessed on 1 March 2018).

16. FEMA. Historic Disaster Response to Hurricane Harvey in Texas. 2017. Available online: [www.fema.gov/news-release/2017/09/22/historicdisaster-response-hurricane-harvey-texas](http://www.fema.gov/news-release/2017/09/22/historicdisaster-response-hurricane-harvey-texas) (accessed on 1 March 2018).
17. Jonkman, S.N.; Godfroy, M.; Sebastian, A.; Kolen, B. Brief communication: Loss of life due to hurricane Harvey. *Nat. Hazards Earth Syst. Sci.* **2018**, *18*, 1073–1078. [[CrossRef](#)]
18. Millera, M.M.; Shirzaei, M. Land subsidence in Houston correlated with flooding from Hurricane Harvey. *Remote Sens. Environ.* **2019**, *225*, 368–378. [[CrossRef](#)]
19. Huang, X.; Runkle, B.R.K.; Isbell, M.; Moreno-García, B.; McNairn, H.; Reba, M.L.; Torbick, N. Rice inundation assessment using polarimetric UAVSAR data. *Earth Space Sci.* **2021**, *8*, e2020EA001554. [[CrossRef](#)]
20. Brisco, B.; Short, N.; van der Sanden, J.; Landry, R.; Raymond, D. A semi-automated tool for surface water mapping with radarsat-1. *Can. J. Remote Sens.* **2009**, *35*, 336–344. [[CrossRef](#)]
21. López-Caloca, A.A.; Tapia-Silva, F.O.; Rivera, G. Sentinel-1 satellite data as a tool for monitoring inundation areas near urban areas in the Mexican tropical wet. In *Water Challenges of an Urbanizing World*; IntechOpen: London, UK, 2018; p. 127.
22. Manjusree, P.; Kumar, L.P.; Bhatt, C.M.; Rao, G.S.; Bhanumurthy, V. Optimization of threshold ranges for rapid flood inundation mapping by evaluating backscatter profiles of high incidence angle sar images. *Int. J. Disaster Risk Sci.* **2012**, *3*, 113–122. [[CrossRef](#)]
23. Yésou, H.; Huber, C.; Haouet, S.; Lai, X.; Huang, S.; de Fraipont, P.; Desnos, Y.L. Exploiting sentinel 1 time series to monitor the largest fresh water bodies in pr china, the Poyang lake. In Proceedings of the 2016 IEEE International Geoscience and Remote Sensing Symposium (IGARSS), Beijing, China, 10–15 July 2016; pp. 3882–3885.
24. Huffman, G.J.; Bolvin, D.T.; Nelkin, E.J. *Day 1 IMERG Final Run Release Notes*; NASA/GSFC: Greenbelt, MD, USA, 2015; p. 9.
25. Cohen, S.; Brakenridge, G.R.; Kettner, A.; Bates, B.; Nelson, J.; McDonald, R.; Huang, Y.F.; Munasinghe, D.; Zhang, J. Estimating floodwater depths from flood inundation maps and topography. *JAWRA J. Am. Water Resour. Assoc.* **2018**, *54*, 847–858. [[CrossRef](#)]
26. Huang, F.; Cao, Z.; Guo, J.; Jiang, S.; Li, S.; Guo, Z. Comparisons of heuristic, general statistical and machine learning models for landslide susceptibility prediction and mapping. *Catena* **2020**, *191*, 104580. [[CrossRef](#)]
27. Janowski, L.; Tylmann, K.; Trzcinska, K.; Rudowski, S.; Tegowski, J. Exploration of Glacial Landforms by Object-Based Image Analysis and Spectral Parameters of Digital Elevation Model. *IEEE Trans. Geosci. Remote Sens.* **2021**, *60*, 4502817. [[CrossRef](#)]
28. Middleton, M.; Nevalainen, P.; Hyvönen, E.; Heikkonen, J.; Sutinen, R. Pattern recognition of LiDAR data and sediment anisotropy advocate a polygenetic subglacial mass-flow origin for the Kemijärvi hummocky moraine field in northern Finland. *Geomorphology* **2020**, *362*, 107212. [[CrossRef](#)]
29. Gebremichael, E.; Molthan, A.L.; Bell, J.R.; Lori, A.S.; Hain, C. Flood Hazard and Risk Assessment of Extreme Weather Events Using Synthetic Aperture Radar and Auxiliary Data: A Case Study. *Remote Sens.* **2020**, *12*, 3588. [[CrossRef](#)]
30. Hashemi, H.; Nordin, M.; Lakshmi, V.; Huffman, G.J.; Knight, R. Bias correction of long-term satellite monthly precipitation product (TRMM 3b43) over the conterminous United States. *J. Hydrometeorol.* **2017**, *18*, 2491–2509. [[CrossRef](#)]
31. Mondal, A.; Lakshmi, V.; Hashemi, H. Intercomparison of trend analysis of multisatellite monthly precipitation products and gauge measurements for river basins of India. *J. Hydrol.* **2018**, *565*, 779–790. [[CrossRef](#)]
32. Le, M.-H.; Lakshmi, V.; Bolten, J.; Bui, D.D. Adequacy of satellite-derived precipitation estimate for hydrological modeling in Vietnam basins. *J. Hydrol.* **2020**, *586*, 124820. [[CrossRef](#)]
33. Lakshmi, V.; Fayne, J.; Bolten, J. A comparative study of available water in the major river basins of the world. *J. Hydrol.* **2018**, *567*, 510–532. [[CrossRef](#)]
34. Kansara, P.; Lakshmi, V. Estimation of land-cover linkage to trends in hydrological variables of river basins in the Indian sub-continent using satellite observation and model outputs. *J. Hydrol.* **2021**, *603*, 126997. [[CrossRef](#)]
35. Dandridge, C.; Fang, B.; Lakshmi, V. Downscaling of smap soil moisture in the Lower Mekong river Basin. *Water* **2020**, *12*, 56. [[CrossRef](#)]
36. Fang, B.; Lakshmi, V.; Bindlish, R.; Jackson, T. AMSR2 soil moisture downscaling using temperature and vegetation data. *Remote Sens.* **2018**, *10*, 1575. [[CrossRef](#)]
37. Fang, B.; Lakshmi, V.; Bindlish, R.; Jackson, T.J. Downscaling of smap soil moisture using land surface temperature and vegetation data. *Vadose Zone J.* **2018**, *17*, 1–15. [[CrossRef](#)]
38. Fang, B.; Lakshmi, V.; Jackson, T.J.; Bindlish, R.; Colliander, A. Passive/active microwave soil moisture change disaggregation using smapvex12 data. *J. Hydrol.* **2019**, *574*, 1085–1098. [[CrossRef](#)] [[PubMed](#)]
39. Fang, B.; Lakshmi, V.; Bindlish, R.; Jackson, T.; Liu, P. Evaluation and Validation of a High Spatial Resolution Satellite Soil Moisture Product over the Continental United States. *J. Hydrol.* **2020**, *588*, 125043. [[CrossRef](#)]
40. Fang, B.; Kansara, P.; Dandridge, C.; Lakshmi, V. Drought monitoring using high spatial resolution soil moisture data over Australia in 2015–2019. *J. Hydrol.* **2021**, *594*, 125960. [[CrossRef](#)]